Reversing tumor to “Hot”

Wang, Shuo; Bai, Yueping; Wang, Dayuan; Zhai, Yunqian; Qiao, Yanqi; Zhao, Xiujie; Yin, Yongmei; Xi, Rimo; Wang, Wei; Zhao, Wei

Published in:
Chemical Engineering Journal

DOI:
10.1016/j.cej.2022.136322

Publication date:
2022

Chemical Engineering Journal 442 (2022) 136322

Contents lists available at ScienceDirect

Chemical Engineering Journal

journal homepage: www.elsevier.com/locate/cej

Reversing tumor to "Hot": A NIR light-triggered carrier-free nanoplatform for enhanced tumor penetration and photo-induced immunotherapy

Shuo Wang [a], Yueping Bai [a], Dayuan Wang [b,c], Yunqian Zhai [d], Yanqi Qiao [a], Xiujie Zhao [a], Yongmei Yin [a], Rimo Xi [a], Wei Wang [e], Wei Zhao [a,*], Meng Meng [a,*]

[a] State Key Laboratory of Medicinal Chemical Biology, College of Pharmacy and KLMDASR of Tianjin, Nankai University, Tongyan Road, Haihe Education Park, Tianjin 300350, China
[b] State Key Laboratory of Medicinal Chemical Biology, Key Laboratory of Functional Polymer Materials, Ministry of Education, Institute of Polymer Chemistry, College of Chemistry, Nankai University, Tianjin 300350, China
[c] University of Groningen and University Medical Center Groningen, Department of Biomedical Engineering, Antonius Deusinglaan 1, 9713 AV Groningen, Netherlands
[d] Department of Pathology, Tianjin Medical University General Hospital, Tianjin 300052, China
[e] Institute of Chemistry & Center for Pharmacy, University of Bergen, Bergen 5020, Norway

ARTICLE INFO

Keywords:
Phototherapy
Immunogenic cell death
Carrier-free nanoplatform
Deep penetration
Distal tumor

ABSTRACT

Immunogenic cell death (ICD) process associated with phototherapy is a promising strategy to inhibit tumor growth and metastasis. To facilitate deep tumor-penetrating photo-immunotherapy, we herein report a near-infrared (NIR) light-triggered carrier-free nanoplatform (IR837) loaded with indocyanine green (ICG) and immune adjuvant R837. The IR837 nanoparticles were prepared as carrier-free nanoassembly and showed good photostability. With the thermal-responsive polydopamine as the shell, the IR837 (~78 nm) can efficiently disassociate into smaller size (~10 nm) under NIR irradiation. Through intravenous injection, IR837 displays prolonged blood circulation and turns into the smaller-sized nanoaggregates to deeply penetrate in the core sites of tumors. The ICD process is then induced and results in dendritic cells (DCs) maturation to initiate the immune response. Eventually, the "cold" tumor would be reversed into the "hot" tumor, promoting the immunotherapeutic outcomes against in-situ and distal tumors under mild temperature (45 °C). In summary, our research provides a prospective intelligent nanodelivery system to perform efficient photothermal immunotherapy against primary and distal tumor growth with hopefully low side effect.

1. Introduction

Tumor progression is highly dependent on the immunosuppressive tumor microenvironment (ITM). Therefore, the "cold" tumors with low immunogenicity cannot stimulate the immune system to kill the tumors by dendritic cells (DCs) or cytotoxic T lymphocytes (CTLs) [1–2]. Consequently, traditional immunotherapeutic strategies, such as immune checkpoint blockade (ICB) and chimeric antigen receptor T cell (CAR-T) therapies [3–4] usually could not achieve satisfactory anti-tumor effect [5–7]. Thus, the conversion of immunosuppressive "cold" tumors into immunoactivated "hot" tumors would be helpful in achieving efficient anti-tumor efficacy.

Increasing findings suggest that immunogenic cell death (ICD) can elicit immune responses [8–9] by releasing damage-associated molecular patterns (DAMPs), including calreticulin (CRT), high mobility group protein B1 (HMGB1) and adenosine triphosphate (ATP) [10]. The CRT can mature dendritic cells (DCs) and engulf dying tumor cells. Besides, HMGB1 and ATP can trigger antigen-specific antitumor T cell responses to kill tumor cells [11]. It has been proposed that most chemotherapeutic and phototherapeutic drugs can cause the ICD process [8]. Chemotherapeutic molecules may cause damage to normal tissues and immune system [12–13]. On the contrary, photothermal therapy holds the advantages in accurate and minimally invasive treatment against cancer [14–16].

It has been found that near-infrared (NIR) FDA-approved photosensitizer, indocyanine green (ICG) can induce ICD pathway [17], which would further activate the immune system to achieve anti-tumor effects [18–20]. However, only photothermal therapy or ICD process cannot sufficiently suppress the tumor growth [21–22], especially against distal or metastatic tumors, since the light can just penetrate within several

* Corresponding authors.
E-mail addresses: wzhao@nankai.edu.cn (W. Zhao), mengmeng@nankai.edu.cn (M. Meng).

https://doi.org/10.1016/j.cej.2022.136322
Received 4 January 2022; Received in revised form 24 February 2022; Accepted 8 April 2022
Available online 12 April 2022

millimeters. Therefore, more consideration was recently focused on combining immunological molecules into the phototherapies via nano-delivery approach by using R837 and CpG as immunostimulated molecules, or IDO inhibitor (IDOi) as immunomodulatory component (Table S1) [23–25]. The immunoadjuvant, TLR7 agonist R837 has been reported to promote DCs maturation, which would favor the ICD process. However, R837 is poorly soluble for systematic administration [26–27]. Considering that intravenous administration has the advantage of rapid absorption with high bioavailability, and the dose is usually much lower than other administration routes [28–29], several nanoparticle systems have been proposed to codeliver R837 with ICG [27,30]. Most of these nanocarriers showed high therapeutic temperature up to nearly 60 °C. However, the excessively high temperature may cause damage to healthy tissues [31–32]. Also, the nanoparticle systems need to be further rationally designed in terms of convenient preparation, responsive release of the payload and low administrated dose.

Hence, to facilitate efficient phototherapy and ICD-induced immunotherapy against tumor growth, we herein propose an intelligent nanocarrier system of ICG and R837 (IR837) (Scheme 1). This nanoformulation contains NIR molecule ICG to guide an image-guided phototherapy and induce thermal-responsive ICD process, TLR7 agonist R837 to stimulate DCs maturation, and thermal-responsive polydopamine layer to improve the stability of the formulation and dissociate the nanoparticles while temperature is elevated. The three components are all FDA-approved, which ensures the good biocompatibility for in vivo administration. The ICG conjugates with R837 through hydrophobic interaction and π–π stacking, then encapsulated with the polydopamine as the shell to obtain the carrier-free IR837 nanoparticles. The IR837 nanoplatform exhibits good stability with the proper size (~78 nm) for intravenous injection. More importantly, the nanoplatform can convert the "cold" tumor into "hot" tumor through the following rationally designed processes. (i): IR837 nanoformulations accumulate in tumor sites through EPR effect, and photothermal treatment of surface tumors is carried out under NIR light irradiation. Meanwhile, as the tumor temperature increases, the nanoformulations would be dissociated into small nanoparticles, which would promote the deep penetration of IR837 in tumor site. (ii) The photothermal treatment induces DAMPs release from dying cells and triggers the ICD process. (iii) The ICD process assisted with R837 would induce DC maturation and enhance the antigen presenting capacity. (iv) The systematic immune response would be activated and $CD8^+$ cells are proliferated in tumor and spleen. (v) The infiltration of DCs and CTL cells in tumor would convert the "cold" tumor into "hot", and the anti-tumor effect will be investigated against both primary and distal tumors.

2. Materials and methods

2.1. Preparation and characterization of IR837 nanoformulation

Typically, 1 mM of ICG in aqueous solution (500 μL) and 1 mM of R837 in DMSO (500 μL) was separately dispersed into ultrapure water (3.98 mL) under stirring (1000 rpm). Then 1 mM of dopamine hydrochloride in aqueous solution (20 μL) was introduced into the solution. After stirring for 1 h, the mixed solution was purified in a dialysis bag (MWCO = 1000 Da) at room temperature for 24 h to remove free molecules. The loading efficiencies of ICG and R837 were determined by UV absorbance on a microplate reader (Tecan, Switzerland) and high performance liquid chromatography (HPLC, Shimadzu LC20, Japan), respectively. The encapsulation efficiency (EE) was then calculated by the following equation: EE (%) = molecule loaded / molecule added × 100%.

The particle size and zeta potential of IR837 were analyzed using a Zeta Sizer (Malvern, UK). The morphology of IR837 was recorded by transmission electron microscope (TEM, FEI Talos, USA).

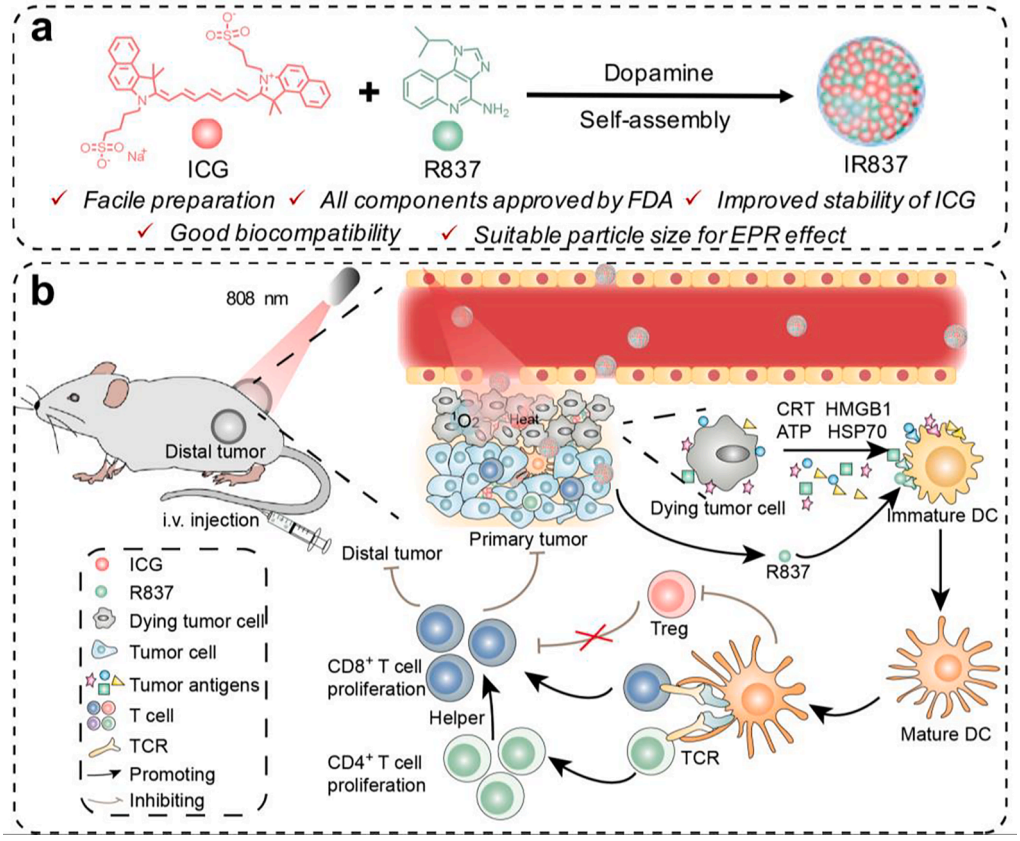

Scheme 1. **(a)** The design and preparation of carrier-free nanoplatform IR837 to codeliver ICG and R837; **(b)** Schematic illustration of the NIR-triggered phototherapy combined with the ICD-based immunotherapy against primary and distal tumors after intravenous injection of IR837.

2.2. Photothermal response and ROS generation ability of IR837

To evaluate photothermal performance of IR837, free ICG and IR837 were treated with the NIR laser irradiation (808 nm, 0.3–1.2 W/cm^2, 5–10 min). The temperature was measured, and the infrared thermal images were recorded using an infrared thermal imaging camera (FLIR, USA). The photothermal conversion efficiencies (PCE, η) were calculated by the equation described in Supplementary Information.

ROS generation was evaluated using a fluorescence probe SOSG. In brief, 10 μM SOSG solution was added into ICG or IR837 solution, followed by irradiation under NIR laser (808 nm, 0.5 W/cm^2, 6 min). The fluorescence emission spectra of SOSG were profiled every 0.5 min to calculate the ROS generation based on the fluorescence intensity of SOSG at 525 nm.

The 2,7-dichlorofluorescein diacetate (DCFH-DA) was used to detect intracellular ROS generation. 4 T1 cells (2×10^5 cells per well) were seeded in 12-well plates and incubated overnight. Then the cells were treated with PBS, free ICG or IR837 (5 μM ICG) for 4 h and then exposed to NIR laser irradiation (808 nm, 0.5 W/cm^2, 5 min). Subsequently, the ROS generation was tracked by fluorescence microscope (Leica, Germany) after DCFH-DA staining.

2.3. Cellular uptake and distribution of IR837 nanoparticles

The cellular uptake of IR837 nanoparticles was studied by confocal laser scan microscope (CLSM). 4 T1 cells were seeded in 35 mm confocal dishes and incubated overnight. Then the cells were treated with ICG or IR837 (containing 10 μM ICG) for 10 h. After washing with PBS, the cells were fixed with 4% paraformaldehyde and the nuclei were stained with DAPI. Images were then acquired using a confocal laser scanning microscope (CLSM, Zeiss LSM 800, Germany). For intracellular trafficking study, the lysosome and nuclei of IR837-treated cells were labeled with Lyso-Tracker and DAPI, respectively.

2.4. Ex vivo tumor penetration of IR837 in 4 T1 tumor spheroids

4 T1 tumor spheroids were prepared and employed to investigate the photo-triggered deep penetration of IR837 in tumor. Briefly, each well of 96-well plates was coated by 1% agarose (50 μL) and then irradiated with UV light for 30 min. After that, the plate was added with 1.0×10^3 4 T1 cells per well. After incubation for 3 days, the spheroids were identified and then treated with IR837 under laser irradiation (808 nm, 0.5 W/cm^2, 5 min). The Z-stack images of spheroids were recorded by CLSM for deep penetration analysis.

2.5. In vitro cytotoxicity assay

MTT assay was performed to evaluate the cytotoxicity of different formulations. 4 T1 cells (5×10^3 cells per well) were seeded into 96-well plates and incubated overnight. After treated with different concentration (0–15 μM) of ICG formulations for 12 h with or without laser irradiation (808 nm, 0.5 W/cm^2, 5 min), the cells were then incubated with the medium containing 20 μL MTT solution. Then the medium was replaced by 150 μL of DMSO, and the microplate reader was used to determine the absorbance of different samples at 562 nm. The relative cell viability was calculated according to the following formula:

$$\text{Relative viability } (\%) = (OD_{Sample} - OD_{PBS}) / (OD_{Blank} - OD_{PBS}) \times 100\%$$

For live/dead cell double staining, 4 T1 cells (1×10^5 cells per well) were seeded into 24-well plates and incubated overnight. After treated with different ICG formulations (5 μM ICG) for 6 h with or without laser irradiation (808 nm, 0.5 W/cm^2, 5 min), the cells were stained with calcein-AM and propidium iodide (PI) solution and then imaged by CLSM. For apoptosis evaluations, the cells treated with different formulations were stained with Annexin V-FITC and PI solution for flow cytometry analysis. The results were then processed by Flowjo software.

2.6. CRT expression, HMGB1 and ATP release from the tumor cells

CRT expression and HMGB1 release were examined by immunofluorescence analysis. 4 T1 cells (2×10^4 cells per dish) were seeded into 35 mm confocal dishes and incubated overnight. Subsequently, the cells were incubated with different formulations (5 μM ICG) for 6 h and then exposed under the laser irradiation (808 nm, 0.5 W/cm^2, 2 min). Then the cells were fixed using 4% paraformaldehyde for 20 min and permeabilized with 0.1% Triton-100 for 15 min. After blocked by 10% goat serum for 1 h, the cells were incubated with primary antibodies (anti-CRT, anti-HMGB1 and anti-HSP70) at 4 °C overnight. The cells were then incubated with Alexa Fluor 488-labeled secondary antibody (1 h) and DAPI (15 min), then washed with PBS for three times. Finally, the cellular fluorescent images were examined by CLSM. For flow cytometry, The cells were collected after blocked by 10% goat serum, then incubated with antibodies of CRT and HSP70 and detected by flow cytometer. For ATP release assay, the cells were treated as indicated above, and the supernatants were used to detect ATP release by a chemiluminescence assay kit.

2.7. In vitro maturation of BMDCs

To investigate in vitro maturation of bone marrow-derived dendritic cells (BMDCs), we isolated BMDCs from the bone marrow of female BALB/c mice, and seeded the BMDCs (1×10^5 cells per well) into 24-well plates. In another 24-well plate, 4 T1 cells (1×10^5 cells per well) were treated with the ICG formulations (5 μM ICG) for 6 h. After irradiated with NIR laser (808 nm, 0.5 W/cm^2, 1 min), the medium supernatants were collected and added into the BMDCs. After 24 h, the BMDCs were stained using anti-mouse antibodies of CD11c-APC, CD80-FITC and CD86-PE to identify the activated BMDCs by flow cytometry.

2.8. Hemolysis test, pharmacokinetics and biodistribution of IR837

For hemolysis test, the fresh blood was collected from tumor-free BALB/c mice (5 to 6 weeks) and the red blood cells (RBCs) were then obtained under centrifugation at 2500 rpm for 10 min, then the RBCs were washed with PBS three times and suspended in PBS. The RBCs were mixed with different concentrations of IR837 for 1 h and then centrifuged. Finally, the supernatant was measured by a microplate reader at 560 nm. For hematology assay, the fresh blood was collected from tumor-free BALB/c mice (5 to 6 weeks) treated with PBS or IR837 for 10 days, and tested using an animal blood cell analyzer (BC-2800Vet).

Tumor-free BALB/c mice (5 to 6 weeks) were divided into two groups and intravenously injected with free ICG and IR837 (1.0 mg ICG/kg), respectively. Then the blood samples were collected from the *retro*-orbital plexus at predetermined time points (0.083, 0.5, 1.167, 3, 7, 12, and 24 h), and the centrifuged at 1500 rpm for 10 min to obtain the plasma. The plasma half life of ICG was measured by relative fluorescence intensity measured on a microplate reader.

The biodistribution of IR837 was studied in 4 T1 tumor-bearing mice. The model was developed by subcutaneously injecting 4 T1 cells (1×10^6 cells per mouse) into the right flank of each female BALB/c mouse (5–6 weeks). When the tumor volume reached about 150 mm^3, the mice were intravenously injected with free ICG or IR837 (1.0 mg ICG/kg). At certain time points (0, 3, 6, 12, 24, and 48 h), the NIR fluorescence signals were recorded using the In Vivo Imaging System (IVIS Spectrum, PerkinElmer, USA). The major organs were collected and imaged at 24 h after injection. For in vivo PTT performance, the thermal images were recorded when the tumor site was irradiated with NIR laser (808 nm, 0.5 W/cm^2, 5 min) after injection.

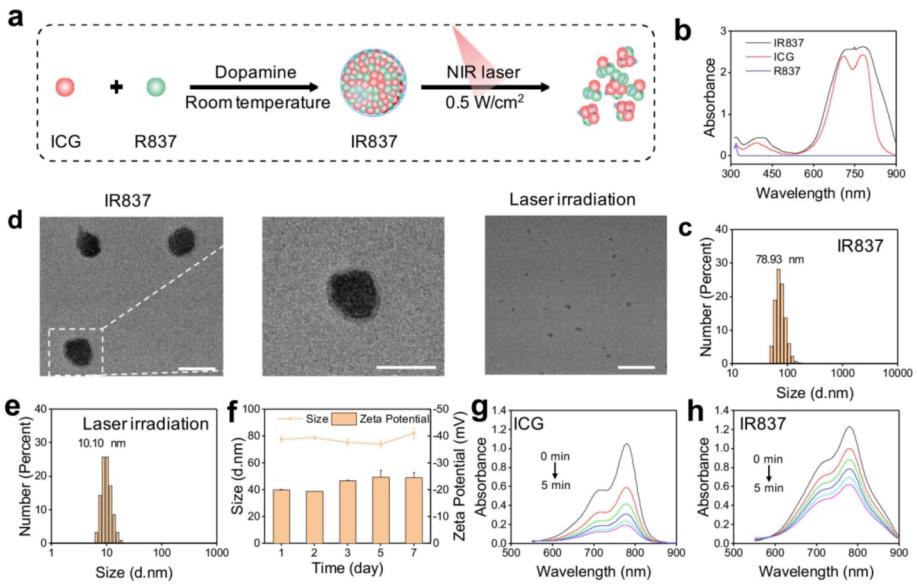

Fig. 1. Preparation and characterization of IR837 nanoplatform. (a) Scheme illustrating of the preparation and disassembly of IR837 nanoformulation. **(b)** UV absorbance spectra for ICG, R837 and IR837. **(c)** Particle size distribution of IR837 solution. **(d)** TEM images of IR837 solution before and after laser irradiation (808 nm, 0.5 W/cm^2, 5 min). Scale bar: 100 nm. **(e)** Particle size distribution of IR837 after laser irradiation. **(f)** Particle size and zeta potential of IR837 after stored at room temperature for 7 days. UV absorbance spectra for ICG **(g)** and IR837 **(h)** treated with laser irradiation for 5 min.

2.9. In vivo tumor inhibition and immunohistochemical assay

The 4 T1-bearing mice model was established as described above. When the tumor volume reached about 100 mm^3, the mice were randomly divided into 6 groups and intravenously injected with different formulations at the ICG dose of 1 mg/kg, then irradiated with NIR laser (808 nm, 0.5 W/cm^2, 5 min). Mice treated with PBS were used as the control group. The weight of the 4 T1-bearing mice were recorded every day, and the tumor volume was calculated according to the formula: Tumor volume = (length × width^2) / 2.

For anti-distal tumor therapy, 1 × 10^6 4 T1 cells per mouse were subcutaneously injected into the left flank of the mice after the injection of primary tumor for 6 days, and the tumor volume on the left flank was measured every day. For hematoxylin and eosin (H&E) staining and immunohistochemistry (IHC) assay, the mice were sacrificed to collect tumors and main organs (liver, heart, lung, kidney and spleen). After

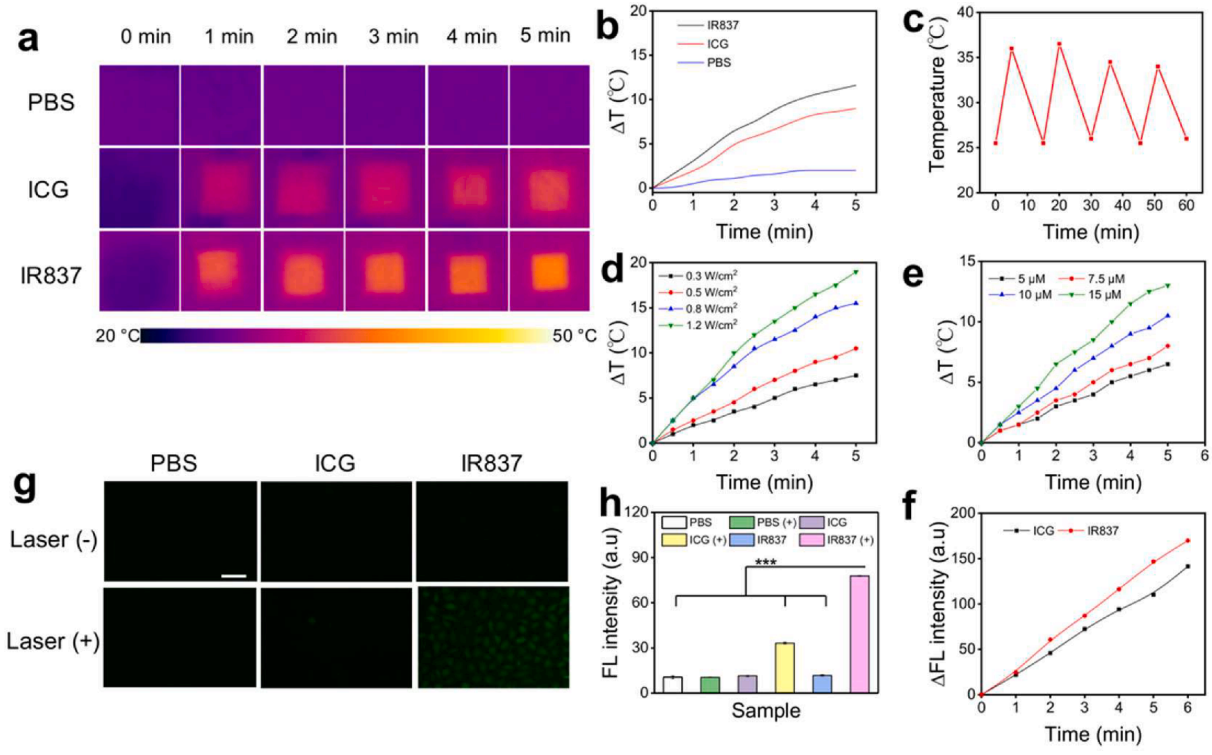

Fig. 2. PTT and PDT performance of IR837 nanoplatform under NIR laser irradiation. (a) Infrared thermal images of PBS, ICG and IR837 (containing 10 μM ICG) under laser irradiation (808 nm, 0.5 W/cm^2, 5 min). **(b)** Temperature profile of different solutions under laser irradiation. **(c)** Temperature changes of IR837 under laser irradiation for four cycles of heat-cooling experiment. **(d)** Temperature profiles of IR837 under different power of laser irradiation. **(e)** Temperature profile of IR837 in different concentration under laser irradiation (0.5 W/cm^2). **(f)** Fluorescence intensity changes of SOSG at 525 nm after incubated with ICG or IR837 under irradiation (0.5 W/cm^2). Fluorescence images **(g)** and mean fluorescence intensity **(h)** of 4 T1 cells stained by DCFH-DA after incubated with various formulations with (+) or without (-) the laser (scale bar: 100 μm, ***$p < 0.001$).

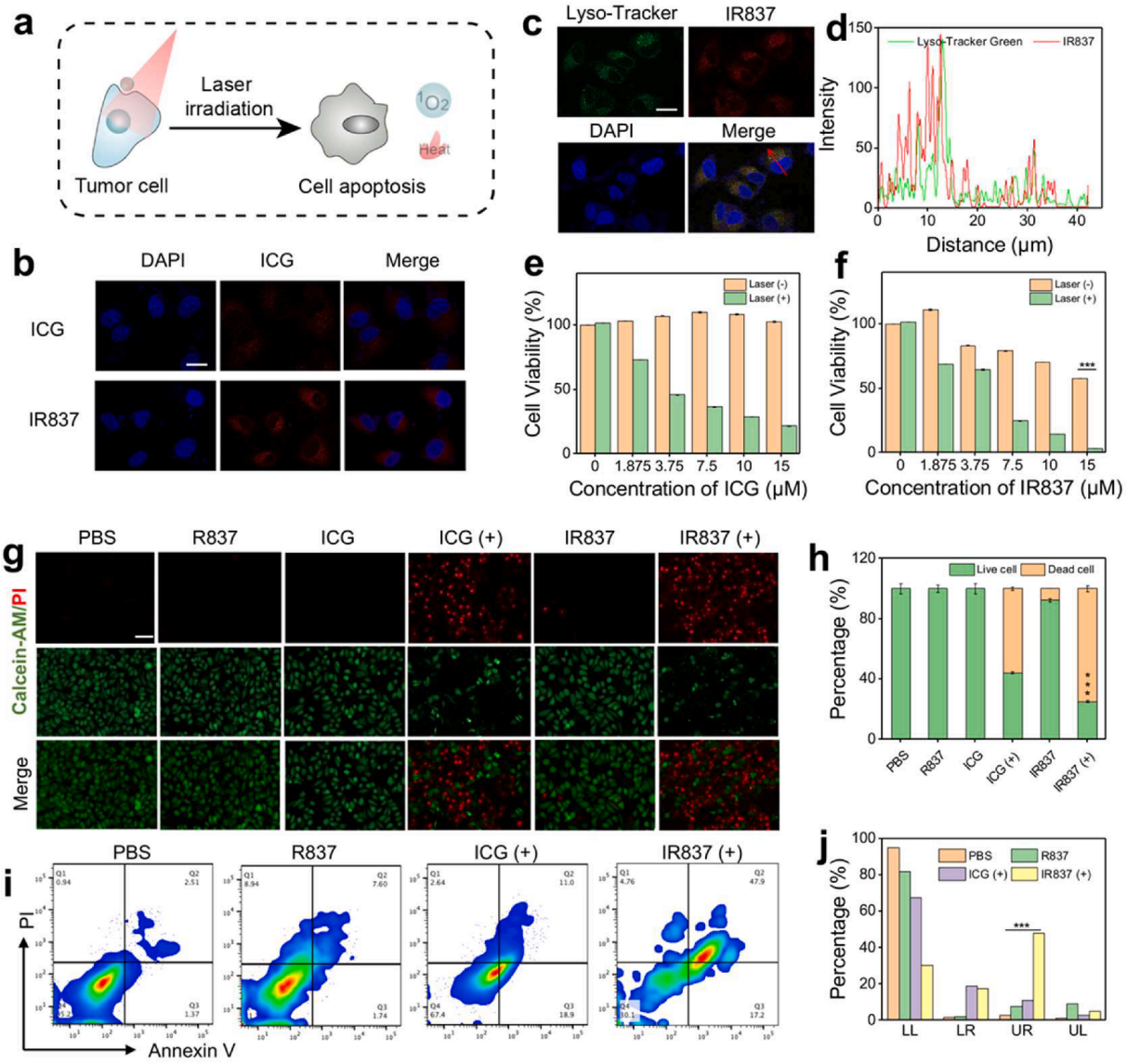

Fig. 3. Cellular uptake and cytotoxicity assay of IR837 nanoplatform. (a) Schematic illustration of the cellular uptake and apoptotic process. **(b)** CLSM images of 4 T1 cells treated with ICG or IR837. Scale bar: 20 μm. **(c)** CLSM images of intracellular co-localization of IR837 with Lyso-Tracker Green in 4 T1 cells and **(d)** the fluorescence correlation between the two dyes. Scale bar: 20 μm. Cell viability of 4 T1 cells after treated with different concentrations of free ICG **(e)** or IR837 **(f)**. $^{***}p < 0.001$. **(g)** Calcein-AM and PI live-dead cell staining of 4 T1 cells after treatment with R837, ICG or IR837 with or without laser irradiation (808 nm, 0.5 W/cm^2, 5 min) and the mean fluorescence intensity **(h)** of each group. Scale bar: 100 μm. $^{***}p < 0.001$. **(i)** Flow cytometry analysis and **(j)** quantitative evaluation of 4 T1 cell apoptosis after treatment with various formulations through Annexin V-FITC/PI staining (LL: lower left; LR: lower right; UR: upper right; UL: upper left). $^{***}p < 0.001$.

weighted, all tumor samples were fixed with 10% formalin solution and embedded in paraffin. Then 5 μm-thick paraffin sections were sliced for H&E and IHC assay. To evaluate the therapeutic biosafety of IR837, the plasma samples were subjected to the hematology analysis of biochemical markers correlated with liver and kidney function according to the instruction of assay kit.

2.10. In vivo evaluation of ICD process and immune response

The ICD process was evaluated by detecting CRT expression, HMGB1, and ATP release in 4 T1 tumor harvested from the tumor-bearing mice in paraffin sections and single-cell suspension. IHC assay was used to analyze the CRT expression and HMGB1 release as described above. The ATP in the cell suspension was analyzed by luminescence assay as illustrated above.

On the 10th day after the phototherapy, we collected the tumors and spleens of the mice to prepare the single-cell suspension. To detect the DCs and T lymphocytes infiltration in tumor site or spleen, we stained the single-cell suspension in tumor or spleen with fluorescent-labeled antibodies of CD11c-APC, CD80-FITC, CD86-PE, CD3-APC, CD4-FITC and CD8-PE, for flow cytometry analysis. The cells of $CD11c^+CD80^+CD86^+$, $CD3^+CD4^+$ and $CD3^+CD8^+$ were recognized to be matured DCs, helper T lymphocytes and cytotoxic T lymphocytes, respectively. Meanwhile, IHC analysis of tumor sections was performed to visualize cytotoxic T lymphocytes and regulatory T lymphocytes according to the quantification of CD8 and CD25, respectively.

3. Results and discussion

3.1. Preparation and characterizations of IR837

The IR837 nanoformulation was prepared through π–π stacking and

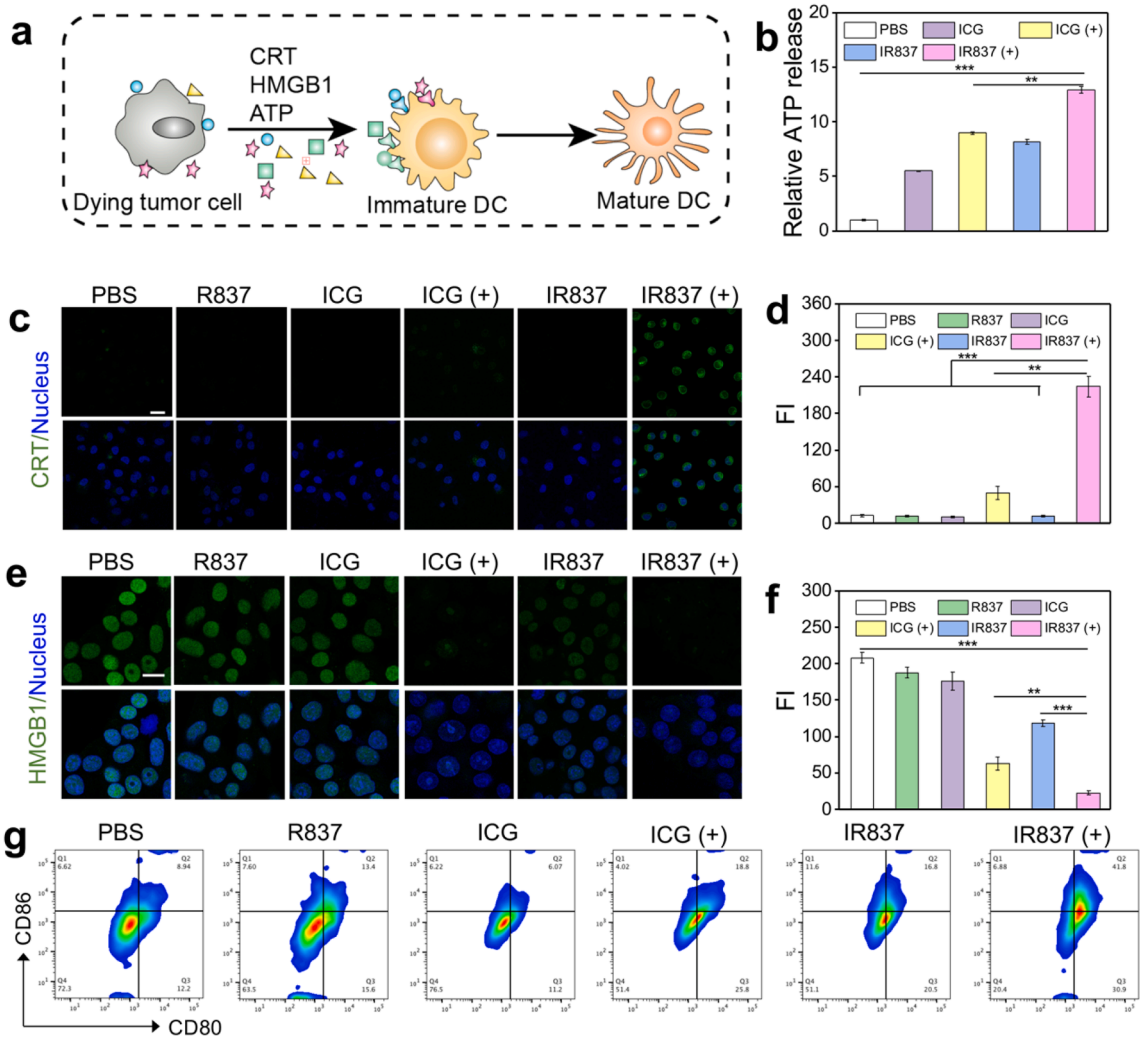

Fig. 4. In vitro ICD effect of IR837 nanoplatform under NIR laser irradiation. (a) Schematic illustration of PTT-induced ICD effect and BMDCs maturation. **(b)** ATP release of 4 T1 cells determined by chemiluminescent assay after treated with ICG or IR837 with or without irradiation (808 nm, 0.5 W/cm^2, 5 min). **(c)** Immunofluorescence images and quantitative analysis of fluorescence intensity **(d)** of CRT in 4 T1 cells treated with R837, ICG or IR837. Scale bar: 20 μm. **(e)** Immunofluorescence staining and quantitative analysis of fluorescence intensity **(f)** of HMGB1 release in 4 T1 cells after treated with various formulations. Scale bar: 20 μm. **(g)** Flow cytometry analysis of BMDCs maturation after incubated with the supernatant of 4 T1 cells in different groups. $^{**}p < 0.01$, $^{***}p < 0.001$.

hydrophobic interaction between ICG and R837, and encapsulated with polydopamine shell to improve the stability and thermal response (Fig. 1a). The UV–vis spectra (Fig. 1b) of IR837 nanoparticles showed the characteristic peaks of R837 and ICG at 325 and 780 nm, respectively. We then optimized the molar ratio of ICG versus R837 based on the results of particle size and encapsulation efficiencies. As shown in Figure S1 and Table S2, the optimal molar ratio of ICG to R837 was determined to be 1:1. Under this condition, the encapsulation efficiencies of ICG and R837 were 41.30% and 28.36%, respectively. The mean diameter of IR837 was 78.93 nm (Fig. 1c; Figure S2a) with homogenous and spherical morphology (Fig. 1d), which would contribute to tumor accumulation through EPR effect. Compared with the nanoparticles without polydopamine (Figure S3), IR837 nanoparticles showed more uniform and stable morphology. After laser irradiation for 5 min (808 nm, 0.5 W/cm^2), the polydopamine shell was dissociated and the IR837 nanoparticles were disparted into smaller (~10 nm) and irregular ones (Fig. 1d–e, Figure S2b), which would favor the deep tumor penetration in vivo.

We then studied the stability of IR837. As seen in Fig. 1f, the particle size and zeta potential of IR837 were very stable when it was stored at room temperature in dark for 7 days. Besides, IR837 remained stable in diluted medium, and the lyophilized IR837 still turned homogeneous after it was resonstited (Figure S4). To further evaluate the photostability, we measured the UV absorbance of ICG and IR837 samples after irradiation for 5 min and found that the absorbance of ICG solution significantly declined, but only slightly decreased for IR837 (Fig. 1g–h; Figure S5), which revealing the good stability of the IR837 during storage and phototherapy.

3.2. *In vitro photoactivity evaluation of IR837*

The in vitro photoactivity was evaluated by measuring the temperature increment and ROS generation under the irradiation (808 nm, 0.5 W/cm^2). As shown in Fig. 2a–b, the temperature increased nearly 9 °C for ICG solution and 12 °C for IR837 nanoparticles (containing 10 μM ICG). Then the photothermal conversion efficiency (PCE) was tested based on the heat-cooling assay [33], and determined to be 47.88% for IR837, which was twice higher than free ICG (23.64%). These results suggested higher PTT efficiency of IR837 formulation (Figure S6a–b, Table S3). In addition, heat-cooling experiments (Fig. 2c) showed that IR837 still exhibited stable photothermal response in the period of three cycles, suggesting the promising potential of IR837 for continuous photothermal therapy. Moreover, the IR837 nanoformulation displayed both concentration-dependent and irradiation intensity-dependent

patterns (Fig. 2d–e).

Next, we tested the PDT effect of IR837 using the singlet oxygen ($^1O_2$) indicator SOSG. As seen in Figure S6c–d, without laser irradiation, there was little fluorescence of SOSG observed at 525 nm for ICG and IR837 group. Upon the irradiation for 6 min, the fluorescence was remarkably increased in both groups (Fig. 2f). Interestingly, the intracellular $^1O_2$ generation (Fig. 2g–h) in IR837-treated cells was nearly 2.5-fold stronger than that in ICG-treated cells, suggesting an enhanced intracellular PDT effect in IR837 group, which was probably induced by the promoted cellular uptake of IR837 than free ICG.

3.3. Cellular uptake and penetration of IR837

To study the cellular uptake of IR837, we incubated 4 T1 cells with different formulations and tracked the intracellular distribution of dyes by confocal laser scanning microscope (CLSM). As shown in Fig. 3a–b, the red fluorescence in IR837-treated cells was significantly stronger than those treated with ICG, and the mean fluorescence intensity of the cells in IR837 group was about 2-fold higher than that of the ICG group (Figure S7), further suggesting the improved cellular uptake of IR837. The cellular uptake of IR837 was monitored at different time intervals (Figure S8) and indicated a time-dependent uptake of IR837. Then the intracellular distribution was explored by co-localization of IR837 emission with lysosome staining probe, Lyso-Tracker Green. The results showed a consistent localization between the two dyes (Fig. 3c–d), which revealed that the IR837 nanoparticles were possibly internalized through endocytosis pathway.

It has been proposed that the nanoparticles with size of ~ 100 nm exhibited high accumulation around the leaky regions of the tumor vasculature, but low penetration into the dense collagen matrix of solid tumor [34]. On the contrary, the nanoformulations with smaller particle size (<20 nm) are believed more favorable in deep tumor penetration [35]. Therefore, we used 4 T1 tumor spheroids as the ex vivo 3D tumor model, and investigated the tumor penetration of IR837 under thermal response of the polydopamine layer. The results showed that in the tumor spheroids treated with IR837 before irradiation, the fluorescence mostly located on the periphery of the tumor spheroids (Figure S9). By contrast, after irradiation, the IR837-treated cells showed stronger fluorescence from the deeper site of 90 μm. This observation clearly demonstrated enhanced penetration capability of IR837 after irradiation, which is probably attributed to the increased temperature in tumor site and sequentially dissociation of IR837.

3.4. Cytotoxicity assay

Next, MTT assay was applied to investigate the cytotoxicity of different formulations in 4 T1 tumor cells. After incubated with ICG and IR837 up to 15 μM without laser applied, the 4 T1 cells remained high viability, suggesting the low cytotoxicity of the IR837 nanoformulation. When the cells were exposed to NIR laser (808 nm, 0.5 W/cm^2, 5 min), the IR837 displayed obvious antitumor efficacy (Fig. 3e–f; Figure S10). The photo-induced antitumor effect was then evaluated using live-dead double staining assay. As seen in Fig. 3g, there was almost no PI fluorescence in the cells without laser irradiation. After exposure to laser irradiation, more cells were dead in IR837 group than ICG group (Fig. 3h), which verified efficient phototoxicity of IR837 over ICG. The flow cytometry results (Fig. 3i–j) demonstrated that the highest apoptosis (65.1%) was observed in IR837 plus irradiation group, which would benefit the occurrence of ICD-induced immune responses.

3.5. In vitro evaluation of ICD-activated BMDCs maturation

Phototherapy has been reported to induce an immunological response through immunogenic cell death (ICD) process (Fig. 4a), which is usually characterized by release of damage associated molecular patterns (DAMPs), such as adenosine triphosphate (ATP), high mobility group box 1 (HMGB1) and heat shock protein 70 (HSP70) from dying tumor cells [36]. Hence, we investigated the phototherapy-induced ICD

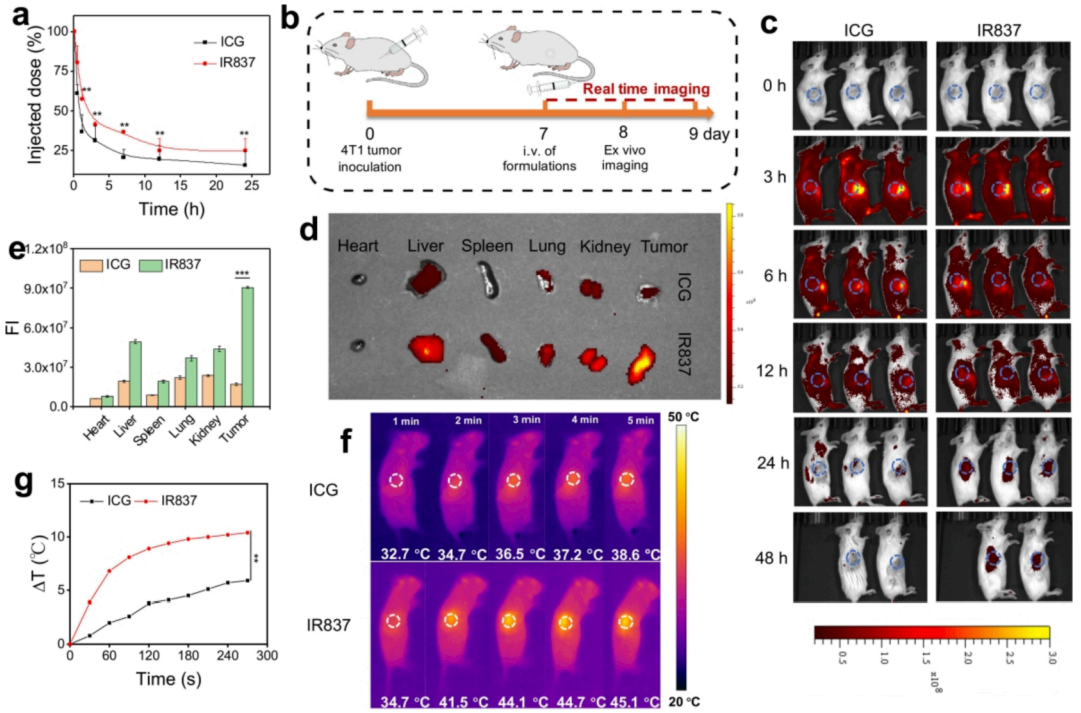

Fig. 5. Pharmacokinetics and in vivo biodistribution of IR837. (a) Pharmacokinetic curves of IR837 in tumor-free female BALB/c mice after the tail vein injection. **(b)** In vivo imaging schedule of ICG or IR837 treated 4 T1-tumor bearing mice. **(c)** In vivo fluorescence images of ICG or IR837 treated 4 T1 tumor-bearing mice within 48 h. **(d)** Fluorescence images and intensity **(e)** of the major organs of 4 T1 tumor-bearing mice 24 h after injected with ICG or IR837 (Ex = 745 nm; Em = 800 nm). **(f)** Infrared thermal images of ICG or IR837 treated 4 T1 tumor-bearing mice under NIR laser irradiation (808 nm, 0.5 W/cm^2, 5 min). **(g)** Temperature profiles of ICG or IR837 treated 4 T1 tumor-bearing mice under NIR laser irradiation, $^{**}p < 0.01$, $^{***}p < 0.001$.

by analyzing CRT expression on the 4 T1 cells incubated with PBS, R837 and ICG formulations (5 μM ICG) using immunostaining analysis and flow cytometry. CLSM results displayed that under irradiation, ICG could slightly induce CRT exposed to the cell surface. However, the CRT expression was significantly promoted in the cells treated with IR837 under irradiation (Fig. 4c–d), and the flow cytometry results (Figure S11) showed similar results with CLSM. Furthermore, the HMGB1 release was evaluated. The immunofluorescence results showed that the green fluorescence of nuclear protein HMGB1 overlapped well with the nucleus in the groups without laser irradiation, indicating little release of HMGB1 from the cells. Under the irradiation, the release of HMGB1 was induced from the nucleus in both ICG and IR837 groups (Fig. 4e), in which the HMGB1 release in IR837 group (87.7%) was 3.0-fold more than ICG group (Fig. 4f). Then, we measured the ATP release, as it serves as chemotaxis reagent to recruit antigen presenting cells (APCs) to facilitate the ICD process. The results showed that the cells treated with IR837 under laser irradiation released more ATP than ICG with irradiation (1.4 fold) and IR837 without irradiation (1.5 fold) (Fig. 4b). Moreover, the expression of HSP70 was significantly up-regulated in IR837 group under irradiation by CLSM and flow cytometry (Figure S12). These results suggested remarkable photothermal-induced ICD process.

As ICD process could promote the maturation and antigen-presenting ability of DCs, we further investigated ex vivo maturation of BMDCs. After isolated from female BALB/c mice [37], BMDCs were incubated with the supernatants of 4 T1 cells pre-treated with different formulations, then characterized by flow cytometry. The cells with $CD11c^{+}CD80^{+}CD86^{+}$ would be defined as matured BMDCs. As shown in Fig. 4g, under the irradiation, significantly more matured BMDCs (41.8%) were acquired in IR837 group than R837 (13.40%) and ICG (18.8%) group (Figure S13), which proving effective maturation of BMDCs through ICD process induced by IR837 with laser.

3.6. *In vivo pharmacokinetics and photothermal response of IR837*

To study the blood biocompatibility of the nanoparticles, we thus performed the hemolysis test. As shown in Figure S14, the hemolysis rate of IR837 with different concentrations was lower than 5.0%. Furthermore, hematology assay of BALB/c mice showed consistent results between PBS and IR837 groups (Table S4). These results suggested good blood compatibility of IR837.

Before the performance of phototherapy, we first investigated the pharmacokinetics of ICG and IR837 after intravenous injection into healthy mice. As shown in Fig. 5a, the ICG showed a half life ($t_{1/2}$) of 5.32 h, while IR837 formulation exhibited a prolonged blood circulation with $t_{1/2}$ of 12.95 h (Figure S15). Subsequently, the tumor accumulation

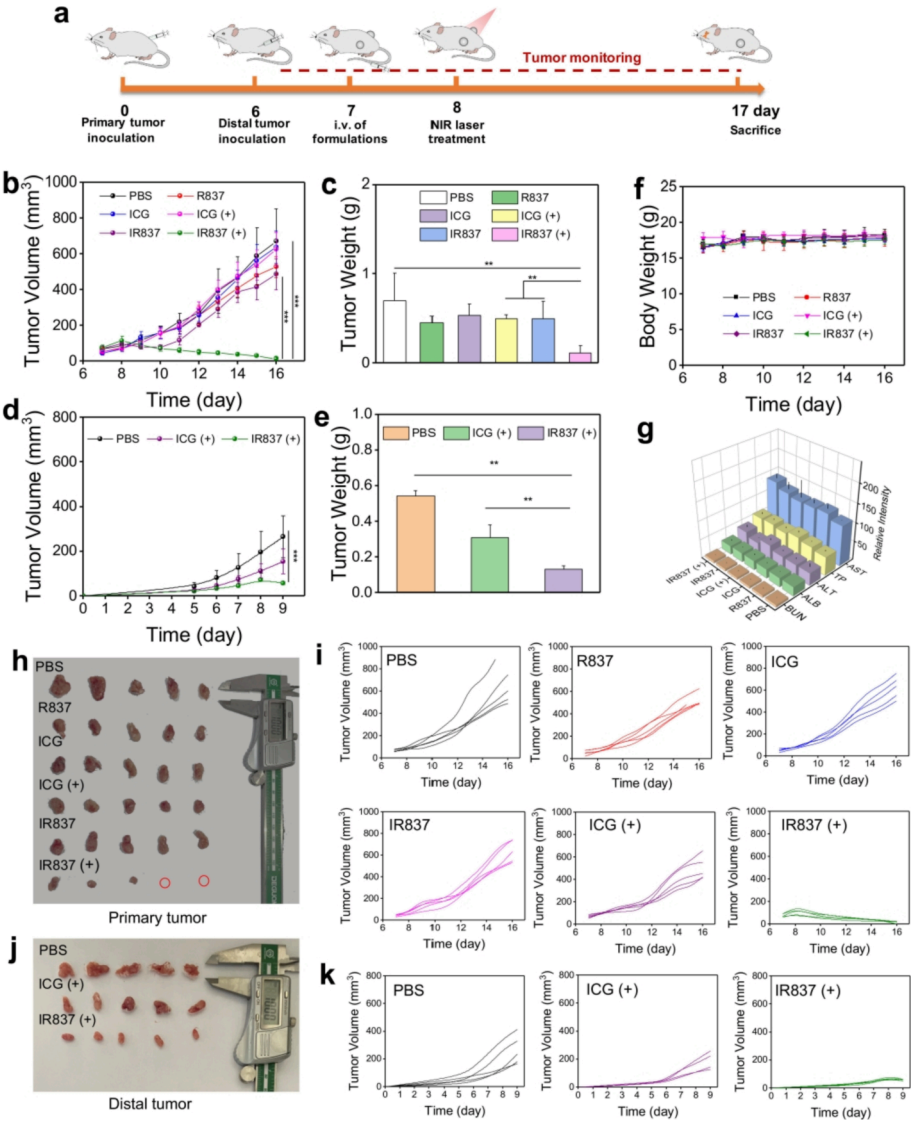

Fig. 6. In vivo photo-induced immunotherapy of IR837 in 4 T1 tumor-bearing mice after intravenously injected with different formulations. (a) Therapeutic schedule of primary and distal tumors of the tumor-bearing mice using IR837. Tumor growth curves of the primary tumors **(b)** and distal tumors **(d)** after treatment with IR837 formulations. $^{***}p < 0.001$. Tumor weight of the primary tumors **(c)** and distal tumors **(e)** of the mice collected on the 17th day. $^{**}p < 0.01$. **(f)** Body weight of the mice after receiving different treatments for 17 days. **(g)** Plasma analysis of AST, TP, ALT, ALB and BUN after different treatments for 17 days. The images of excised primary **(h)** and distant tumor **(j)** after the treatment. The individual primary **(i)** and distant **(k)** tumor growth curves of the tumor-bearing mice after the treatments.

of IR837 in 4 T1 tumor-bearing mice was monitored (Fig. 5b), and in vivo images showed that the ICG fluorescence distributed in multiple parts of the body within 12 h. After 12 h, the fluorescence gradually became weak. However, the fluorescence in tumor site was continuously bright in IR837 group. Even over 24 h after injection, the fluorescence was still strong and mainly located at the tumor site, indicating a prolonged tumor retention of IR837 (Fig. 5c). After 24 h, the tumors and major organs were collected and imaged (Fig. 5d). As seen in ICG group, the fluorescence in liver and kidney was significantly stronger than that in tumor, suggesting that ICG was metabolized rapidly through the liver and kidney. In contrast, the IR837 fluorescence in tumor was obviously stronger than other organs, and was about 6-fold higher than ICG group (Fig. 5e), which further confirmed the enhanced tumor accumulation of IR837. Moreover, IR837-treated tumor showed stronger fluorescence after NIR irradiation (Figure S16), which suggested enhanced penetration of IR837 after irradiation benefited from the thermal-induced dissociation.

Next, we recorded the infrared thermal images of 4 T1 tumor-bearing mice intravenously injected with IR837, and irradiated by laser 24 h after the intravenous injection. Considering the extremely high temperature (above 50 °C) could generate immunosuppressive cytokine, immune escape of tumor cells [38] as well as damage to normal tissues [39–40], we used a low NIR laser density (0.5 W/cm^2) in the phototherapeutic experiments. As shown in Fig. 5f–g, the tumor temperature in ICG group increased by about 5.9 °C (up to 38.6 °C), and rose to 45.1 °C in IR837-treated mice. The mild temperature in IR837 group would favor the phototherapy with hopefully less harmful to healthy tissues.

3.7. Photo-induced antitumor efficacy of IR837 in tumor-bearing mice

For in vivo anti-tumor phototherapy, we established the 4 T1 tumor-bearing mice model by subcutaneous injection of 4 T1 cells (1×10^6 cells per mouse) into the right flank. When the tumor volume reached about 100 mm^3, the mice were randomly divided and treated by PBS, R837, ICG and IR837 (1.0 mg/kg of ICG) with or without NIR laser irradiation (808 nm, 0.5 W/cm^2, 5 min) at 24 h after the injection (Fig. 6a). Then the tumor volume and body weight of the mice were monitored in the following 17 days. The tumor growth was slightly inhibited in ICG or R837 groups, while obviously inhibited in the IR837 plus laser group (Fig. 6b). The results indicated that phototherapy or immunotherapy alone cannot achieve efficient antitumor effect. As expected, synergetic effect of photo-induced immunotherapy was observed in IR837 group. At the 17th day, the tumor weight of mice in IR837 group with irradiation was 5.9-fold lighter than that of PBS group (Fig. 6c, h and i). Administration of IR837 with irradiation achieved the tumor suppression rate as high as 83.83% and even two mice in this group were finally tumor-free. Hematoxylin-eosin (H&E) staining results showed the tumor cell damage and nuclear deformation in IR837 with irradiation (Figure S17), confirming that the IR837 showed great potential in the

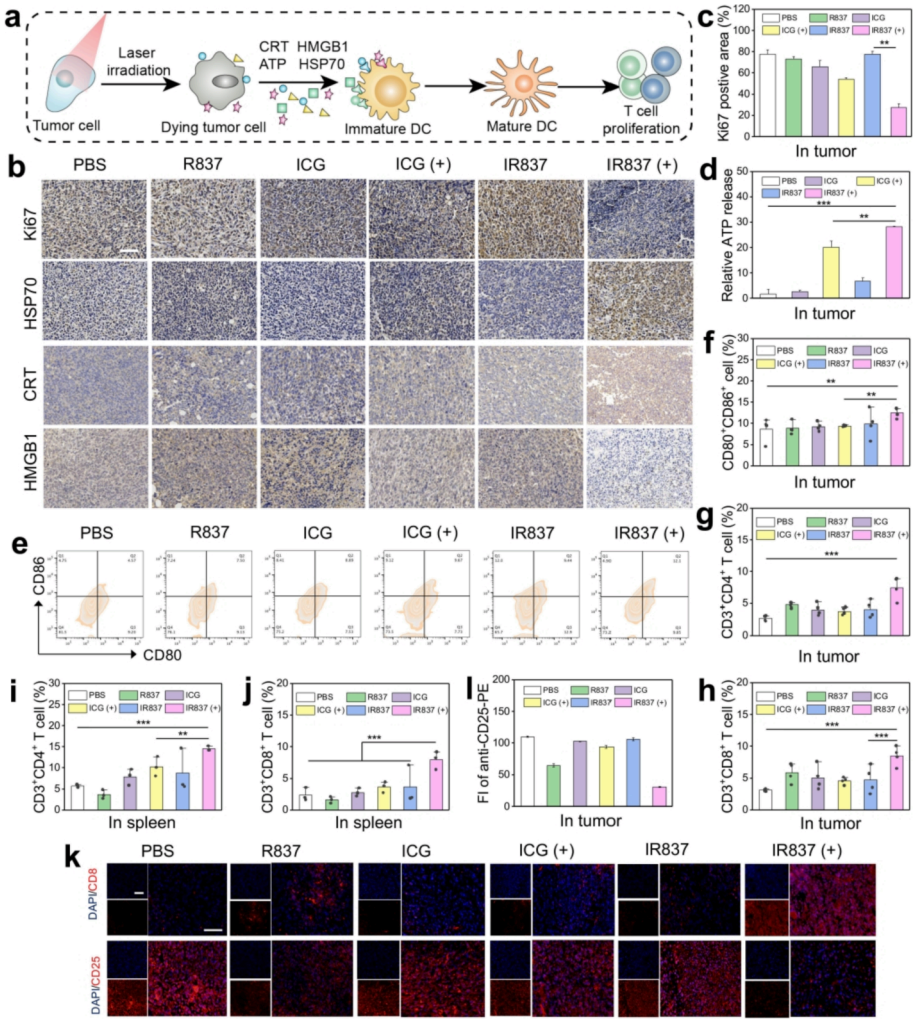

Fig. 7. ICD process and systematic immune activation induced by photothermal immunotherapy in 4 T1 tumor-bearing mice after intravenously injected with different formulations. (a) Schematic illustration of the immune system activation. **(b)** IHC staining of apoptosis and ICD process markers (Ki67, HSP70, CRT and HMGB1) in the tumor sections. Scale bar: 100 μm. **(c)** Quantitative analysis of Ki67 protein. **(d)** Relative release of ATP in single-cell suspension of the tumors. **(e)** Percentage of mature DC ($CD80^+CD86^+$) detection in the tumor site through flow cytometry. **(f)** Quantitative analysis of mature DC ($CD80^+CD86^+$). Helper T lymphocytes ($CD3^+CD4^+$) **(g)** and cytotoxic T lymphocytes (CTLs) ($CD3^+CD8^+$) **(h)** in tumor site after photo-immunotherapy. Helper T lymphocytes ($CD3^+CD4^+$) **(i)** and CTLs ($CD3^+CD8^+$) **(j)** in spleen after photo-immunotherapy. **(k)** Immunofluorescence (IF) staining of CTLs ($CD8^+$) and regulatory T lymphocytes (T_{reg}, $CD25^+$) in the tumor sections. Scale bar: 100 μm. **(l)** Fluorescence quantitative analysis of $CD25^+$ cells. $^{**}p < 0.01$, $^{***}p < 0.001$.

antitumor treatment. Overall, even under low dose (1 mg/kg) of ICG and mild temperature elevation to about 45 °C, the anti-tumor effect was still obvious. To investigate whether the phototherapy would effectively lead to antitumor immunotherapy, we established distal tumor model on BALB/c mice by subcutaneous injection of 4 T1 cells (1×10^6 cells per mouse) into the left flank. As shown in Fig. 6d–e, j–k, after injected with IR837 under irradiation on primary tumor, the growth of the abscopal tumors was also inhibited, which suggested that the administration of IR837 with laser irradiation could lead to effective treatment against distal tumor growth. During the treatment, there was almost no weight fluctuation of the mice (Fig. 6f). Furthermore, the plasma biochemical markers indicating liver and kidney function were determined, such as alanine aminotransferase (ALT), blood urea nitrogen (BUN) and aspartate transaminase (AST), and results showed that level of the markers was almost similar in IR837 and PBS group (Fig. 6g, Figure S18), conforming the low side effect of IR837 administration. The H&E staining (Figure S19) results suggested good biocompatibility of IR837.

3.8. Verification of the antitumor immune response

The immune-potentiating effects of IR837 nanoplatform were then clarified in 4 T1 tumor-bearing mice (Fig. 7a). The immunohistochemical (IHC) staining results showed that the expression of ki67 protein in the tumor of IR837 irradiation group was significantly reduced (27.7%), indicating that proliferation of tumor cells was inhibited (Fig. 7b–c). After that, ICD process was studied by measuring the release of DAMPs (CRT, HSP70, HMGB-1 and ATP) in dying tumor cells (Fig. 7b, d). As HSP70 protein could effectively activate dendritic cells (DCs), HSP70 protein was significantly upregulated in IR837 group with irradiation, suggesting the possibility of immune response induced by HSP70. Then, the IHC examination of the tumor sections verified the in vivo CRT exposure and HMGB1 release, and the chemiluminescence assay of single cell suspension confirmed the ATP release. These results demonstrated the occurrence of ICD process induced by the phototherapy.

Next, we investigated the ability of IR837 to stimulate in vivo DC maturation ($CD11c^+$, $CD80^+$, $CD86^+$). The tumor tissue was harvested to prepare the single cell suspension for flow cytometry, and the results (Fig. 7e–f) showed that neither free ICG nor R837 could stimulate DC maturation. However, mature DCs was found in IR837 group under irradiation, indicating that the phototherapy-induced ICD process by IR837 could effectively activate immune response in tumor site.

As the matured DCs could activate cytotoxic T lymphocytes (CTLs) and helper T lymphocytes, and induce systematic immune effect [41–42], we studied immune cells infiltration at tumor site and systematic immune activation in spleen of the mice on the 10th day after the injection. As shown in Fig. 7g–h, IR837 administration with irradiation induced the highest level of $CD3^+CD4^+$ helper T cells and $CD3^+CD8^+$ CTLs in tumor (Figure S20a), and the infiltration of these immune cells would benefit the reversion of “cold” tumor into “hot”. Moreover, IR837 group with irradiation led to the highest proportion of CTLs and helper T lymphocytes in the spleen (Fig. 7i–j, Figure S20b), confirming that injection of IR837 followed by laser could effectively activate systematic immune. To visualize the $CD8^+$ and $CD25^+$ T cells in tumor tissue, we then performed immunofluorescence staining of tumor sections and found that IR837 under irradiation efficiently activated $CD8^+$ CTLs in tumor (Fig. 7k). Immunofluorescence results showed that IR837 could significantly downregulate the percentage of $CD25^+$ T_{reg} cells under light exposure (Fig. 7l), indicating the remodeled tumor microenvironment. All results above demonstrated that IR837 could activate the immune system by inducing ICD under irradiation and turn the “cold” tumor into “hot” with systematic anti-tumor efficiency.

4. Conclusion

In this study, we designed a photothermal-induced immunotherapy nanoplatform IR837 for efficiently and deeply penetrating anti-tumor treatment. IR837 nanoparticles were conveniently constructed based on a coordination interaction between ICG and R837, and stayed stabe within one week. After administration, the IR837 nanoformulation held a prolonged half-life (2.4 times than free ICG). The nanoplatform was dissociated into smaller nanoparticles in response to high temperature, which greatly favors the deep penetration of ICG into the solid tumor under mild temperature (45 °C). The immune system was then activated through ICD process aided with R837. Finally, the immunotherapy successfully converted “cold” tumor into “hot” tumor against both primary and distal tumor. To sum up, our design provides a promising synergistic therapy of photothermal treatment with immunotherapy in anti-tumor therapy with efficient outcome and good biocompatibility.

Declaration of Competing Interest

The authors declare that they have no known competing financial interests or personal relationships that could have appeared to influence the work reported in this paper.

Acknowledgments

This work was supported by the National Key R&D Program of China (2018YFA0507204), International Science & Technology Cooperation Program of China (No. 2015DFR40460), and National Natural Science Foundation of China (No. 81573390).

Appendix A. Supplementary data

Supplementary data to this article can be found online at https://doi.org/10.1016/j.cej.2022.136322.

References

[1] A.D. Waldman, J.M. Fritz, M.J. Lenardo, A guide to cancer immunotherapy: from T cell basic science to clinical practice, Nat. Rev. Immunol. 20 (2020) 651–668.
[2] S. Gao, X. Yang, J. Xu, N. Qiu, G. Zhai, Nanotechnology for boosting cancer immunotherapy and remodeling tumor microenvironment: the horizons in cancer treatment, ACS Nano 36 (2021), 101035.
[3] A. Ribas, J.D. Wolchok, Cancer immunotherapy using checkpoint blockade, Science 359 (6382) (2018) 1350–1355.
[4] N.T. Nguyen, K. Huang, H. Zeng, J.I. Jing, R. Wang, S. Fang, J. Chen, X. Liu, Z. Huang, M.J. You, A. Rao, Y. Huang, G. Han, Y. Zhou, Nano-optogenetic engineering of CAR T cells for precision immunotherapy with enhanced safety, Nat. Nanotechnol. 16 (12) (2021) 1424–1434.
[5] S.J. Turley, V. Cremasco, J.L. Astarita, Immunological hallmarks of stromal cells in the tumour microenvironment, Nat. Rev. Immunol. 15 (11) (2015) 669–682.
[6] C. Sautès-Fridman, F. Petitprez, J. Calderaro, W.H. Fridman, Tertiary lymphoid structures in the era of cancer immunotherapy, Nat. Rev. Cancer 19 (6) (2019) 307–325.
[7] L. Chen, H. Qin, R. Zhao, X. Zhao, L. Lin, Y. Chen, Y. Lin, Y. Li, Y. Qin, Y. Li, S. Liu, K. Cheng, H. Chen, J. Shi, G.J. Anderson, Y. Wu, Y. Zhao, G. Nie, Bacterial cytoplasmic membranes synergistically enhance the antitumor activity of autologous cancer vaccines, Sci. Transl. Med. 13 (2021) eabc2816.
[8] G. Kroemer, L. Galluzzi, O. Kepp, L. Zitvogel, Immunogenic cell death in cancer therapy, Annu. Rev. Immunol. 31 (1) (2013) 51–72.
[9] L. Wang, R. Guan, L. Xie, X. Liao, K. Xiong, T.W. Rees, Y.U. Chen, L. Ji, H. Chao, An ER-targeting Iridium(III) complex that induces immunogenic cell death in non-small-cell lung cancer, Angew. Chem. Int. Ed. 60 (9) (2021) 4657–4665.
[10] F. Wang, D. Xu, H. Su, W. Zhang, X. Sun, M.K. Monroe, R.W. Chakroun, Z. Wang, W. Dai, R. Oh, H. Wang, Q. Fan, F. Wan, H. Cui, Supramolecular prodrug hydrogelator as an immune booster for checkpoint blocker–based immunotherapy, Sci. Adv. 6 (18) (2020) eaaz8985.
[11] J. Nam, S. Son, K.S. Park, W. Zou, L.D. Shea, J.J. Moon, Cancer nanomedicine for combination cancer immunotherapy, Nat. Rev. Mater. 4 (6) (2019) 398–414.
[12] J.I. Hare, T. Lammers, M.B. Ashford, S. Puri, G. Storm, S.T. Barry, Challenges and strategies in anti-cancer nanomedicine development: An industry perspective, Adv. Drug Deliv. Rev. 108 (2017) 25–38.
[13] S. Sen, S. Hufnagel, E.Y. Maier, I. Aguilar, J. Selvakumar, J.E. DeVore, V.M. Lynch, K. Arumugam, Z. Cui, J.L. Sessler, J.F. Arambula, Rationally designed redox-active Au(I) N-heterocyclic carbene: an immunogenic cell death inducer, J. Am. Chem. Soc. 142 (2020) 20536–20541.
[14] Y. Liu, P. Bhattarai, Z. Dai, X. Chen, Photothermal therapy and photoacoustic imaging via nanotheranostics in fighting cancer, Chem. Soc. Rev. 48 (7) (2019) 2053–2108.

[15] Y. Chen, Y. Gao, Y. Chen, L. Liu, A. Mo, Q. Peng, Nanomaterials-based photothermal therapy and its potentials in antibacterial treatment, J. Control. Release 328 (2020) 251–262.
[16] J.P. Celli, B.Q. Spring, I. Rizvi, C.L. Evans, K.S. Samkoe, S. Verma, B.W. Pogue, T. Hasan, Imaging and photodynamic therapy: mechanisms, monitoring, and optimization, Chem. Rev. 110 (2010) 2795–2838.
[17] Y. Jia, X. Wang, D. Hu, P. Wang, Q. Liu, X. Zhang, J. Jiang, X. Liu, Z. Sheng, B. Liu, H. Zheng, Phototheranostics: Active targeting of orthotopic glioma using biomimetic proteolipid nanoparticles, ACS Nano 13 (2019) 386–398.
[18] P. Zhao, M. Wang, M. Chen, Z. Chen, X. Peng, F. Zhou, J. Song, J. Qu, Programming cell pyroptosis with biomimetic nanoparticles for solid tumor immunotherapy, Biomaterials 254 (2020), 120142.
[19] M. Li, D.I. Xie, X. Tang, C. Yang, Y. Shen, H. Zhou, W. Deng, J. Liu, S. Cai, L.I. Bai, Y. Wang, Phototherapy facilitates tumor recruitment and activation of natural killer T cells for potent cancer immunotherapy, Nano Lett. 21 (14) (2021) 6304–6313.
[20] Z. Di, B. Liu, J. Zhao, Z. Gu, Y. Zhao, L. Li, An orthogonally regulatable DNA nanodevice for spatiotemporally controlled biorecognition and tumor treatment, Sci. Adv. 6 (2020) eaba9381.
[21] S. Zhang, J. Wang, Z. Kong, X. Sun, Z. He, B. Sun, C. Luo, J. Sun, Emerging photodynamic nanotherapeutics for inducing immunogenic cell death and potentiating cancer immunotherapy, Biomaterials 282 (2022), 121433.
[22] S. Wang, Z. Liu, Y. Tong, Y. Zhai, X. Zhao, X. Yue, Y. Qiao, Y. Liu, Y. Yin, R. Xi, W. Zhao, M. Meng, Improved cancer phototheranostic efficacy of hydrophobic IR780 via parenteral route by association with tetrahedral nanostructured DNA, J. Control. Release 330 (2021) 483–492.
[23] Y. Liu, Y. Lu, X. Zhu, C. Li, M. Yan, J. Pan, G. Ma, Tumor microenvironment-responsive prodrug nanoplatform via co-self-T assembly of photothermal agent and IDO inhibitor for enhanced tumor penetration and cancer immunotherapy, Biomaterials 242 (2020), 119933.
[24] L. Qin, J. Cao, K. Shao, F. Tong, Z. Yang, T. Lei, Y. Wang, C. Hu, C.S. Umeshappa, H. Gao, N.A. Peppas, A tumor-to-lymph procedure navigated versatile gel system for combinatorial therapy against tumor recurrence and metastasis, Sci. Adv. 6 (2020) eabb3116.
[25] Q. Chen, L. Xu, C. Liang, C. Wang, R. Peng, Z. Liu, Photothermal therapy with immune-adjuvant nanoparticles together with checkpoint blockade for effective cancer immunotherapy, Nat. Commun. 7 (2016) 13193.
[26] D.J.A. Crommelin, P. van Hoogevest, G. Storm, The role of liposomes in clinical nanomedicine development. What now? Now what? J. Control. Release 318 (2020) 256–263.
[27] J. Xu, L. Xu, C. Wang, R. Yang, Q.I. Zhuang, X. Han, Z. Dong, W. Zhu, R. Peng, Z. Liu, Near-infrared-triggered photodynamic therapy with multitasking upconversion nanoparticles in combination with checkpoint blockade for immunotherapy of colorectal cancer, ACS Nano 11 (5) (2017) 4463–4474.
[28] A. Mansurov, J. Ishihara, P. Hosseinchi, L. Potin, T.M. Marchell, A. Ishihara, J.-M. Williford, A.T. Alpar, M.M. Raczy, L.T. Gray, M.A. Swartz, J.A. Hubbell, Collagen-binding IL-12 enhances tumour inflammation and drives the complete remission of established immunologically cold mouse tumours, Nat. Biomed. Eng. 4 (5) (2020) 531–543.
[29] L. Zhang, Y. Zhou, X. Chai, Z. Yang, N. Pang, Y. Du, X. Qi, Excipient-free prodrug-based three-in-one nanoparticles co-deliver diversified agents to amplify tumor therapy, Chem. Eng. J. 435 (2022), 134880.
[30] M. Wang, Y. Li, M. Wang, K. Liu, A.R. Hoover, M. Li, R.A. Towner, P. Mukherjee, F. Zhou, J. Qu, W.R. Chen, Synergistic interventional photothermal therapy and immunotherapy using an iron oxide nanoplatform for the treatment of pancreatic cancer, Acta Biomater. 138 (2022) 453–462.
[31] D. Yoo, H. Jeong, S.-H. Noh, J.-H. Lee, J. Cheon, Magnetically triggered dual functional nanoparticles for resistance-free apoptotic hyperthermia, Angew. Chem. Int. Ed. 52 (49) (2013) 13047–13051.
[32] G. Gao, X. Sun, X. Liu, Y. Jiang, R. Tang, Y. Guo, F. Wu, G. Liang, Intracellular nanoparticle formation and hydroxychloroquine release for autophagy-inhibited mild-temperature photothermal therapy for tumors, Adv. Funct. Mater. 31 (2021) 2102832.
[33] X. Zhao, S. Long, M. Li, J. Cao, Y. Li, L. Guo, W. Sun, J. Du, J. Fan, X. Peng, Oxygen-dependent regulation of excited-state deactivation process of rational photosensitizer for smart phototherapy, J. Am. Chem. Soc. 142 (3) (2020) 1510–1517.
[34] C. Wong, T. Stylianopoulos, J. Cui, J. Martin, V.P. Chauhan, W. Jiang, Z. Popović, R.K. Jain, M.G. Bawendi, D. Fukumura, Multistage nanoparticle delivery system for deep penetration into tumor tissue, Proc. Natl. Acad. Sci. USA 108 (6) (2011) 2426–2431.
[35] J. Wang, W. Mao, L.L. Lock, J. Tang, M. Sui, W. Sun, H. Cui, D. Xu, Y. Shen, The role of micelle size in tumor accumulation, penetration, and treatment, ACS Nano 9 (7) (2015) 7195–7206.
[36] L. Galluzzi, A. Buqué, O. Kepp, L. Zitvogel, G. Kroemer, Immunogenic cell death in cancer and infectious disease, Nat. Rev. Immunol. 17 (2) (2017) 97–111.
[37] K. Sun, J. Hu, X. Meng, Y. Lei, X. Zhang, Z. Lu, L. Zhang, Z. Wang, Reinforcing the induction of immunogenic cell death via artificial engineered cascade bioreactor-enhanced chemo-immunotherapy for optimizing cancer immunotherapy, Small 17 (37) (2021) 2101897.
[38] G. Gao, Y. Jiang, Y. Guo, H. Jia, X. Cheng, Y. Deng, X. Yu, Y. Zhu, H. Guo, W. Sun, X. Liu, J. Zhao, S. Yang, Z. Yu, F.M.S. Raya, G. Liang, F. Wu, Enzyme-mediated tumor starvation and phototherapy enhance mild-temperature photothermal therapy, Adv. Funct. Mater. 30 (2020) 1909391.
[39] X. Li, J.F. Lovell, J. Yoon, X. Chen, Clinical development and potential of photothermal and photodynamic therapies for cancer, Nat. Rev. Clin. Oncol. 17 (11) (2020) 657–674.
[40] X. Dong, R. Cheng, S. Zhu, H. Liu, R. Zhou, C. Zhang, K. Chen, L. Mei, C. Wang, C. Su, X. Liu, Z. Gu, Y. Zhao, A heterojunction structured $WO_{2.9}$-WSe_2 nanoradiosensitizer increases local tumor ablation and checkpoint blockade immunotherapy upon low radiation dose, ACS Nano 14 (5) (2020) 5400–5416.
[41] F. Zhou, B. Feng, H. Yu, D. Wang, T. Wang, Y. Ma, S. Wang, Y. Li, Tumor microenvironment-activatable prodrug vesicles for nanoenabled cancer chemoimmunotherapy combining immunogenic cell death induction and CD47 blockade, Adv. Mater. 31 (2019) 1805888.
[42] G. Yang, L. Xu, Y. Chao, J. Xu, X. Sun, Y. Wu, R. Peng, Z. Liu, Hollow MnO_2 as a tumor-microenvironment-responsive biodegradable nano-platform for combination therapy favoring antitumor immune responses, Nat. Commun. 8 (2017) 902.